Chinese Journal of Aeronautics, (2023), **36**(6): 128–139

Chinese Society of Aeronautics and Astronautics
& Beihang University

Chinese Journal of Aeronautics

cja@buaa.edu.cn
www.sciencedirect.com

Ion thruster accelerator grid erosion mechanism under extreme conditions of cylindrical erosion and chamfer erosion

Guangqing XIA [a,b,c], Jiahui LI [a,b], Chang LU [a,b,c,*], Hai GENG [d], Vladimir A. SAETCHNIKOV [e], Juan LI [d], Yanlong WANG [d]

[a] *State Key Laboratory of Structural Analysis, Optimization and CAE Software for Industrial Equipment, Dalian University of Technology, Dalian 116024, China*
[b] *Key Laboratory of Advanced Technology for Aerospace Vehicles of Liaoning Province, Dalian University of Technology, Dalian 116024, China*
[c] *Collaborative Innovation Center of Micro & Nano Satellites of Hebei Province, North China Institute of Aerospace Engineering, Langfang 065000, China*
[d] *Science and Technology on Vacuum Technology and Physics Laboratory, Lanzhou Institute of Physics, Lanzhou 730000, China*
[e] *Physics and Aerospace Technology Department, Belarusian State University, Minsk 220030, Belarus*

Received 20 May 2022; revised 26 June 2022; accepted 18 September 2022
Available online 22 March 2023

KEYWORDS

Accelerator grid;
Charge Exchange (CEX) ions;
Erosion;
IFE-PIC-MCC;
Ion propulsion

Abstract In this paper, the abnormal experimental phenomenon on barrel erosion under extreme working conditions in the ultra-long life experiment (> 10000 h) of ion thruster ion optics is studied by the Immersed-Finite-Element Particle-In-Cell Monte-Carlo-Collision (IFE-PIC-MCC) method and the grid erosion evaluation model. The transport process of beam ions and Charge Exchange (CEX) ions in the grid system, and the characteristics and mechanisms of the aperture barrel erosion under extreme erosion conditions (i.e. the cylindrical erosion and chamfer erosion) were systematically studied. Thanks to the advantage of the IFE method for dealing with complex boundaries in structured mesh, the aperture barrel erosion morphology of the accelerator grid is reconstructed accurately based on the experimental results. The results show that, with the evolution of working conditions, the mechanism of the aperture barrel erosion changes significantly, which relies heavily on the accelerator grid morphology. The change of the accelerator grid aperture barrel morphology has a significant effect on the behavior of CEX ions, and only affects the local electric field distribution, but has no effect on the upstream plasma sheath. As the erosion progresses, the erosion position moves downstream along the grid aperture axis direction, and

* Corresponding author.
E-mail address: changlu@dlut.edu.cn (C. LU).
Peer review under responsibility of Editorial Committee of CJA.

Production and hosting by Elsevier

https://doi.org/10.1016/j.cja.2023.03.036

the erosion range becomes narrower. Regardless of the erosion phase, the erosion rate of the CEX ions located downstream of the decelerator grid is the largest. The erosion rate is related to the mean incident energy and angle, and their variation is closely related to the position and trajectory of CEX ions.

1. Introduction

Electric propulsion technology is developing rapidly,[1,2] among which the ion thruster has been widely employed due to its advantages of high efficiency and high specific impulse,[3] and has become one of the hotspots in the research field of electric propulsion technology. The life of the ion thruster is an important performance parameter. The accelerator grid erosion caused by the Charge Exchange (CEX) ions is one of the main reasons that limit the life of the thruster. CEX ions are generated by the charge exchange collisions between beam ions and neutral propellant gas escaping from the discharge chamber. These CEX ions are attracted to the negatively charged accelerator grid, and most hit with sufficient energy to sputter material from the grid. This will ultimately lead to the structural failure of the grids, which will in turn make the entire thruster fail.

In order to accurately predict grid life, many researchers have carried out a lot of numerical studies on the erosion mechanism of ion thruster accelerator grid. For example, Peng et al. studied the accelerator grid erosion by CEX ions utilizing Particle-In-Cell (PIC) and Direct-Simulation-Monte-Carlo (DSMC) methods.[4] Boyd and Crofton calculated the accelerator grid erosion caused by CEX ions collision using fluid, PIC and DSMC methods.[5] Emhoff and Boyd established a two-dimensional axisymmetric numerical simulation model to effectively forecast the life of the NEXT ion thruster optics.[6] Wang et al. developed a fully-three-dimensional particle simulation model to study the grid erosion characteristics.[7] Kafafy and Wang developed the Hybrid-Grid Immersed-Finite-Element Particle-In-Cell (Hybrid-Grid IFE-PIC) method to study the dynamic behavior of beams ions in the ion optics.[8–10] Cao et al. studied the generation and movement characteristics of CEX ions that cause accelerator grid aperture barrel erosion using the IFE-PIC method.[11] Previous studies on the erosion characteristics of the accelerator grid mainly focused on the cylindrical erosion process, and most existing research results show that the accelerator grid erosion rate does not change with the working time, which is generally constant.

However, Brophy[12] and Wirz et al.[13] discovered that the barrel erosion rate can have a dramatical decrease as the accelerator grid aperture barrel is constantly eroded. Also, they found that, after about 10000 h, with the decrease of erosion rate, a special barrel erosion occurs, that is the so-called chamfer erosion. The chamfer erosion is an abnormal phenomenon that occurs under extreme conditions with the greatly distorted accelerator grid aperture barrel morphology. Its erosion characteristics are totally different from those in the early working stage of an ion thruster. At this stage, the erosion rate becomes very low, and it seems that the grid aperture barrel erosion disappears, while the focusing state of beam ions does not change significantly. Hence this phenomenon can have a significant impact on the evaluation of the grid life. However, the characteristics and mechanisms of the chamfer erosion are still not clear, and need to be further studied.

To more accurately predict the service life of the whole grid, this paper makes an effort to clarify the aperture barrel erosion mechanism and characteristics under extreme conditions. Since the generation mechanism of the aperture barrel erosion in this case relies heavily on the accelerator grid aperture barrel morphology, the erosion morphologies were reconstructed based on the experimental results. Then the beam extraction characteristics and CEX ions motion information were simulated with the three-dimensional Immersed-Finite-Element Particle-In-Cell Monte-Carlo-Collision (IFE-PIC-MCC) method. The erosion characteristics such as CEX ion impact current density, energy, angle and erosion rate were obtained through grid erosion valuation model. By reproducing the generation position and trajectory of CEX ions in different regions, the erosion mechanisms of the accelerator grid are analyzed. All results were compared with those at the beginning of the accelerator grid life.

The remainder of this paper is organized as follows. In Section 2, the reconstruction method of erosion morphology, physical model and simulation settings, IFE-PIC-MCC method and grid erosion valuation model are introduced. Section 3 presents the simulation results and discussion. In Section 4, the conclusions are drawn.

2. Computational model

2.1. Erosion morphology reconstruction

From the Beginning-Of-Life (BOL) to the End-Of-Life (EOL), the accelerator grid aperture geometry changes as shown in Fig. 1. The barrel erosion process of accelerator grid can be divided into three phases.[13] Due to differences in grid processing methods, the grid holes are not cylindrical. Taking chemical etching process as an example, the hole geometry will be cusped-shaped.[12] In the first phase, the thruster has just begun to work, CEX ions mainly erode the cusps of the accelerator grid aperture barrel. This process is called cusp erosion. In the second phase, due to the erosion of CEX ions, the diameter

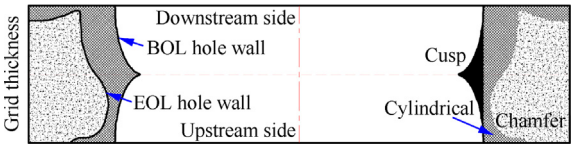

Fig. 1 Accelerator grid aperture barrel geometry at BOL and EOL.

will continue to expand, but the grid aperture morphology will remain basically unchanged until the diameter increases to the final diameter. Hence this process is called cylindrical erosion. In the third phase, CEX ions only erode the downstream area of the accelerator grid, and a chamfer will be formed at the downstream end of the accelerator grid aperture. This process is called chamfer erosion. In this phase, the minimum aperture diameter does not change any more. Only the downstream end of the accelerator grid aperture is enlarged.

In order to analyze the erosion characteristics and generation mechanism at the end of life of the accelerator grid, it is essential to reconstruct the erosion morphology of the accelerator grid aperture. First, the appropriate erosion conditions should be selected. In this paper, the last stage of the cylindrical erosion process and a certain stage of the chamfer erosion process are selected. In the cylindrical erosion phase, the accelerator grid aperture morphology remains cylindrical until the final stage of the cylindrical erosion, when the minimum diameter of the accelerator grid aperture morphology appears. After the chamfer erosion of the accelerator grid occurs, the accelerator grid has a high probability of failure, so any stage in the chamfer erosion phase can be selected to characterize the characteristics and generation mechanism of the chamfer erosion. In order to compare the above two extreme conditions, without considering the cusp erosion phase (the existence of cusp erosion largely depends on the processing method of the accelerator grid, so this paper does not consider cusp erosion), the beginning of the cylindrical erosion phase is also selected. To sum up, the conditions selected to reconstruct the erosion morphology are: the initial and final stages of cylindrical erosion (Case 1 and Case 2), and a certain period of chamfer erosion (Case 3).

Next, the erosion morphologies under the three conditions will be reconstructed. In the initial and final stages of the cylindrical erosion, the accelerator grid aperture morphology remains cylindrical. According to the experimental data of the Lanzhou Institute of Physics, the accelerator grid erosion morphology in these two periods is directly reconstructed. Different from the above two cases, the reconstruction of the chamfer erosion morphology is more complicated and is mainly divided into the following three steps. The first step is to draw the actual erosion profile curve of the accelerator grid aperture according to the experimental data. The second step is to discretize the actual erosion morphology of the accelerator grid aperture. There are three important features in the actual erosion morphology: upstream chamfer, downstream chamfer, and minimum aperture location. In the discrete process, these three features must be preserved, so the non-equidistant dispersion method is used here. To preserve upstream and downstream chamfers, these parts should be discretized with a small thickness. The actual erosion profile curve at the position of the minimum aperture has a smaller curvature, and a large thickness is used to discretize, but the actual erosion profile curve used for the upstream and downstream parts of the minimum aperture has a larger curvature, so a smaller thickness is used for discretization. At other positions, considering the computational efficiency, it is sufficient to use a large thickness to discretize. According to the above analysis, the accelerator grid aperture is split into 8 parts along the thickness direction of the grid, that is, the Accelerator Grid 1 (AG1) to the Accelerator Grid 8 (AG8), as shown in Fig. 2. AG4 is the accelerator grid segment with the minimum aperture radius. A straight line is drawn along the midpoint of the width of each accelerator grid segment. They will intersect the actual erosion profile curve and form eight intersections, that is, Point 1 (IP1) to Point 8 (IP8). Finally, the aperture of each segment (r_{a1} to r_{a8}) is obtained.

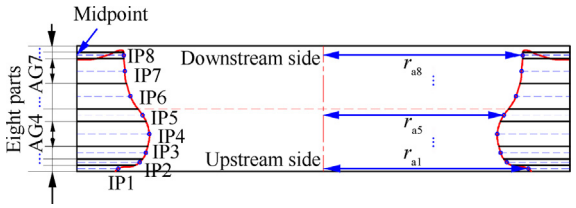

Fig. 2 Dispersion of erosion morphology.

The third step is to complete the reconstruction of the accelerator grid chamfer erosion morphology according to the discrete apertures. The reconstruction results are shown in Fig. 3.

2.2. Physical model and simulation setting

The grid aperture of the ion thruster has a hexagonal structure, that is, six apertures are evenly distributed around one aperture. In order to make the calculation domain contain all the geometric information of the ion optical system, the two-quarter apertures model is used in this paper. The schematic diagram is shown in Fig. 4.

The ion optics comprises three grids: the screen grid, the accelerator grid, and the decelerator grid. Among them, the accelerator grid has three reconstructed erosion morphologies. The schematic diagram of the calculation domain is shown in Fig. 5. In the figure, r_s and r_d represent the radius of the screen grid and the decelerator grid hole respectively, and r_{a4} represents the minimum radius of the accelerator grid hole. The simulation domain mainly has three regions, namely the upstream quasi-neutral plasma region, the beam ion extraction region and the downstream quasi-neutral plasma region.

In order to improve the calculation accuracy and avoid errors caused by the large difference in the magnitude of each parameter in the calculation process, dimensionless processing for all data is adopted. For the dimensionless reference quantities, one can refer to Table 1.[14] The aperture and thickness of the screen grid and the decelerator grid, and the grid spacing can be found in Ref.[15] Table 2 lists the normalized geometric parameters of the grid system, where r_a represents the initial radius of the accelerator grid hole. Since cusp erosion is not considered in this paper, r_a is the radius of Case 1. Table 3 lists the normalized geometric parameters of the accelerator grid in the chamfer erosion phase, where the meanings of r_{a1} to r_{a8} are shown in Fig. 2. The thickness of each segment of the accelerator grid is denoted as t_{a1} to t_{a8}. In the chamfer erosion phase, the minimum aperture diameter does not change any more.

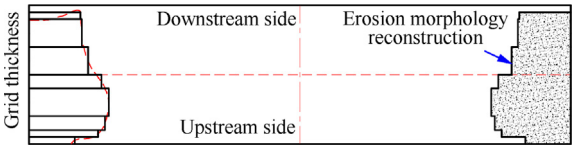

Fig. 3 Erosion morphology reconstruction results.

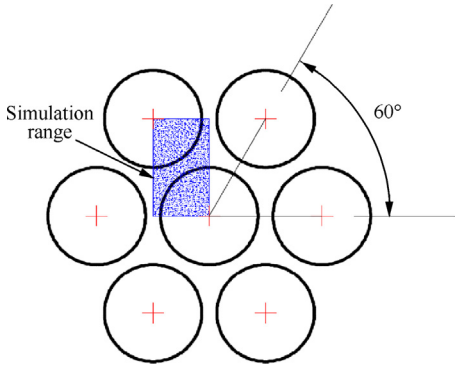

Fig. 4 Schematic diagram of simulation domain.

Therefore, the accelerator grid hole radius of Case 2 is the minimum radius of the chamfered erosion, that is r_{a4}. The normalized data of each grid voltage is shown in Table 4.

For boundary conditions, the potential of the upstream boundary meets the Dirichlet boundary condition, while the others meet the Neumann boundary condition, that is $\frac{\partial \Phi}{\partial n} = 0$ V/m, where Φ is the potential and n is the direction of the boundary normal. When a particle hits the surface of $z = 0$ and $z = z_{max}$, all information of this particle will be deleted. When a particle hits the other four surfaces, it will be reflected back to the simulation domain.

The mesh length in the x,y, and z directions of the simulation domain needs to be less than the Debye length, which is related to the electron temperature and the plasma number density. The mesh is divided according to the different upstream plasma number density n_0, and the division method is shown in Table 5, where Δz is the length of the mesh in the z-direction, n_x, n_y and n_z denotes the number of mesh nodes in the x,y and z directions respectively.

2.3. IFE-PIC-MCC method

The PIC[16,17] method is a kinetic method for simulating low temperature plasmas. The basic idea of this method is to obtain the position and velocity of each particle by simulating the motion of particle, thereby calculating all macroquantities. The MCC method is used for treating collisions between neutral atoms and charged ions. The electric field is solved by the IFE method. The combination of the IFE method and the PIC-MCC method can effectively solve different types of interface problems on structured meshes independent of the interface. The flowchart of the IFE-PIC-MCC method is shown in Fig. 6.

The initialization of the model mainly includes the set-up of simulation domain, mesh and boundary conditions. Afterwards, the simulation environment is established by setting the incident conditions of particles. Then the PIC-MCC loop is carried out. In the particle motion solution, the leap-frog method[18] is used to solve Newton's second law for higher accuracy. Particles in motion will collide with neutral gas atoms. Neutral atoms are set to be uniformly distributed in the simulation domain and obey the law of ideal gas. The number density of neutral atoms can be obtained by[19]

$$n_n = 4\frac{I\gamma}{ev_nA_a} \tag{1}$$

where n_n is the atom density, I is the beam currents, γ is the ratio of atom to ion flow rate, e is the unit charge, v_n is the atom velocity, and A_a is the outlet area of atoms.

The cross-sections[20] of CEX collisions between atoms and ions are obtained as

$$\sigma_T(v_i) = (k_1 \ln v_i + k_2)^2 \tag{2}$$

where $\sigma_T(v_i)$ is the cross-section of CEX collisions; k_1 and k_2 are the collision section coefficients, $k_1 = -0.8821 \times 10^{-10}$s and $k_2 = 15.1262 \times 10^{-10}$m; v_i is the relative velocity between ions and atoms.

The null collision method[21] is used to deal with the charge exchange collision. First, the maximum collision frequency μ_m of all ions is calculated as

$$\mu_m = \max_x [n_n(x_i)] \max_v [\sigma_T(v_i)v_i] \tag{3}$$

where $n_n(x_i)$ is the atom density at x_i.

Then the maximum value of the collision probability P_{null} can be obtained by using the maximum value of the collision frequency,

$$P_{null} = 1 - \exp(-\mu_m \Delta t) \tag{4}$$

where Δt is the time step.

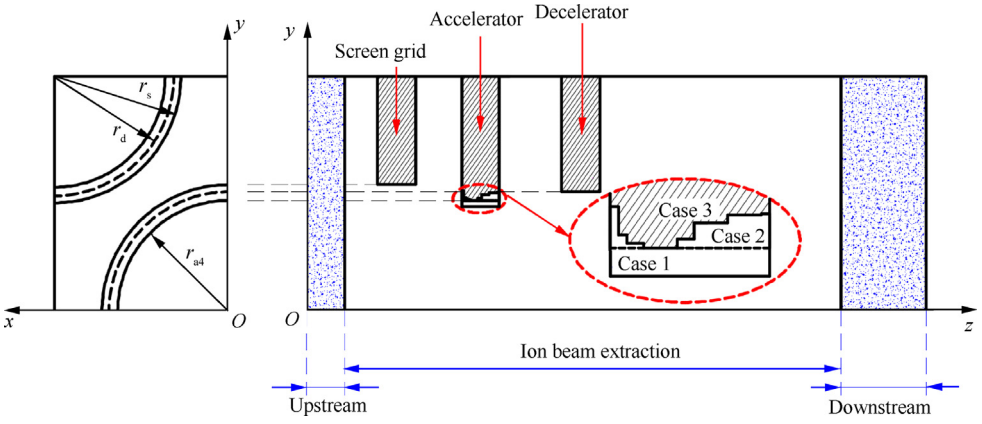

Fig. 5 Schematic diagram of computational domain.

Table 1 Reference parameters[14].

Reference parameter	Value
Charge (C)	1.6022×10^{-19}
Mass (kg)	2.18×10^{-25}
Time step (s)	2.74×10^{-8}
Length (m)	5.2566×10^{-5}
Velocity ($m \cdot s^{-1}$)	1917.4
Number density (m^{-3})	1.0×10^{17}
Potential (V)	5
Temperature (eV)	5
Vacuum permittivity ($F \cdot m^{-1}$)	8.85×10^{-12}

Table 2 Normalized geometrical parameters of grid system.

Normalized parameter	Value
Screen-aperture radius r_s	18.07
Screen-grid thickness t_s	7.61
Accelerator-aperture radius r_a	10.46
Accelerator-grid thickness t_a	9.51
Decelerator-aperture radius r_d	12.37
Decelerator-grid thickness t_d	9.51
Screen-accelerator grid gap l_{sa}	19.02
Accelerator-decelerator grid gap l_{ad}	19.02

Table 3 Normalized geometrical parameters of accelerator grid in chamfer erosion.

Normalized parameter	Value
Accelerator-aperture radius r_{a1}	15.06
Accelerator-grid thickness t_{a1}	0.48
Accelerator-aperture radius r_{a2}	13.50
Accelerator-grid thickness t_{a2}	0.48
Accelerator-aperture radius r_{a3}	13.04
Accelerator-grid thickness t_{a3}	0.95
Accelerator-aperture radius r_{a4}	12.80
Accelerator-grid thickness t_{a4}	1.9
Accelerator-aperture radius r_{a5}	13.30
Accelerator-grid thickness t_{a5}	0.95
Accelerator-aperture radius r_{a6}	14.17
Accelerator-grid thickness t_{a6}	1.9
Accelerator-aperture radius r_{a7}	14.58
Accelerator-grid thickness t_{a7}	1.9
Accelerator-aperture radius r_{a8}	14.66
Accelerator-grid thickness t_{a8}	0.48

Finally, determine whether a collision occurs by selecting a random number. After the collision, the charge of ions is distributed to the mesh nodes by the volume weight distribution method.

In the IFE method,[22,23] a three-dimensional IFE space is initiated and created. In this step, the whole simulation domain will be meshed into cuboid blocks. One cuboid block is then divided into five tetrahedrons. The standard linear basis function is used on each typical non-interface tetrahedron element, while the slice basis function is used in the interface element. Then the stiffness matrix and the right hand vector are assembled with the boundary conditions. Finally, the linear equations are solved, and the potential distribution is obtained.

Table 4 Grid voltage normalized data.

Normalized parameter	Value
Screen grid voltage	280
Accelerator grid voltage	−44
Decelerator grid voltage	0

Table 5 Mesh parameters.

Plasma number density	Mesh length	
	Δz (m)	$n_x \times n_y \times n_z$
$n_0 \leq 1.0$	5.2566×10^{-5}	$27 \times 27 \times 281$
$1.0 < n_0 \leq 2.0$	2.6283×10^{-5}	$53 \times 53 \times 401$

After the electric field is obtained, the force of particles is calculated. When the steady state is reached, the potential distribution and CEX ion information are output to calculate the grid erosion. Otherwise, the next loop is entered.

2.4. Grid erosion valuation

CEX ions are attracted to the negatively charged accelerator grid, and most hit with sufficient energy to sputter material from the grid. The sputtering yield $Y(E,\theta)$ expressed the number of material atoms bombarded by each ion impacting the accelerator grid, which can be given by[24]

$$Y(E,\theta) = Y(E) \cdot Y(\theta) \tag{5}$$

where $Y(E)$ is the normal sputtering yield, and $Y(\theta)$ is the angular sputtering yield. The material of the grid system is molybdenum, and the formula of $Y(E)$ and $Y(\theta)$ can be obtained according to Ref.[25] as follows:

$$Y(E) = \begin{cases} -7.297 \times 10^{-7} E^2 + 2.515 \times 10^{-3} E - 0.1866 & E \leqslant 1000 \text{ eV} \\ -5.559 \times 10^{-8} E^2 + 1.090 \times 10^{-3} E + 0.4778 & E > 1000 \text{ eV} \end{cases} \tag{6}$$

$$Y(\theta) = \begin{cases} 1 + 0.252\theta + 0.6\theta^2 + 0.6\theta^3 & \theta \leqslant 0.698 \text{ rad} \\ -0.057 + 1.9 \exp\left[-\left(\frac{\theta - 0.8201}{0.401}\right)^2\right] & \theta > 0.698 \text{ rad} \end{cases} \tag{7}$$

where E is the incident energy, and θ is the incident angle.

The erosion depth per unit time of a point on the grid surface impacted by incident ions is called erosion rate, which is expressed by R_E[7]

$$R_E = \frac{JY(E,\theta)M}{e\rho} \tag{8}$$

where J is impingement current density, M is the mass of the grid material atoms, and ρ is the density of grid material. The impingement current density formed on the grid surface can be calculated by[26]

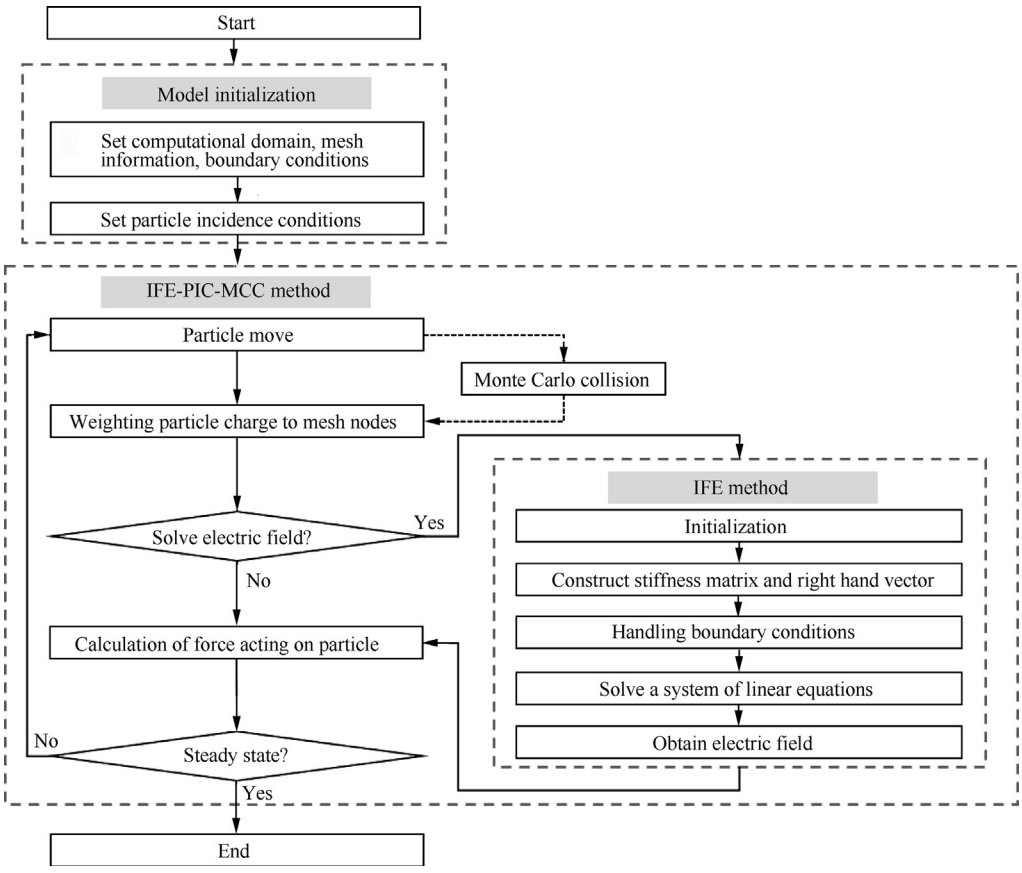

Fig. 6 Flowchart of IFE-PIC-MCC method.

$$J = \frac{eN}{S} \tag{9}$$

where S is a small area, N is the number of ion impacting S.

3. Simulation results and analysis

3.1. Beam extraction characteristics under extreme conditions

The number density distribution of the ions (n_i) is presented in Fig. 7, where the CEX collision is considered in the lower part and not considered in the upper part. All number density data were dimensionless. In the three cases, all beam ions are kept well focused, which can be seen in the upper part of Fig. 7. In other words, the transformation of the Accelerator grid Erosion Morphology (hereinafter referred to as AEM) has no effect on the beam ions. However, in the lower part of Fig. 7, the behavior of CEX ions changes significantly in three cases. In Case 1, that is, the initial stage of cylindrical erosion, most of the CEX ions erode the aperture of the accelerator grid, and the erosion range covers the entire aperture. In Case 2, the final stage of cylindrical erosion, the erosion location of CEX ion moves downstream, and the erosion range becomes smaller. In Case 3, during chamfer erosion, CEX ions avoid the minimum diameter in the AEM, but erode the downstream corners of the accelerator grid, and the erosion range is further compressed. It can be found that as the erosion progresses, the erosion position of the CEX ion moves downstream along the grid aperture axis direction, and the erosion range becomes narrower.

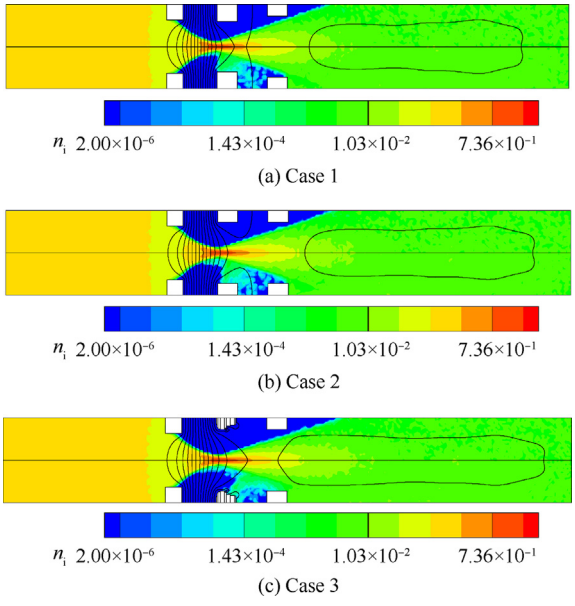

Fig. 7 Number density distribution of beam ions and CEX ions.

Fig. 8 presents the potential distribution of sheath structure and the grid for the three cases. In order to more clearly

observe the variation of the potential under different AEM, the potential distribution of the grid aperture axis is taken out, as shown in Fig. 9. The potential data in Fig. 8 and Fig. 9 are dimensionless. Combining Fig. 8 with Fig. 9, we can see that the potential distribution of sheath structure of the three cases does not change much. In simpler terms, the transformation of the AEM only affects the local electric field distribution. Furthermore, comparing Fig. 8(a) and Fig. 8(b), we can see that, in the cylindrical erosion phase, the transformation of AEM only affects the potential distribution around the accelerator grid. But in the chamfer erosion phase, the special erosion morphology allows this effect to spread to the downstream area of the decelerator grid, which can be seen in Fig. 8(c). We can conclude that as the erosion progresses, the negative potential area gradually decreases.

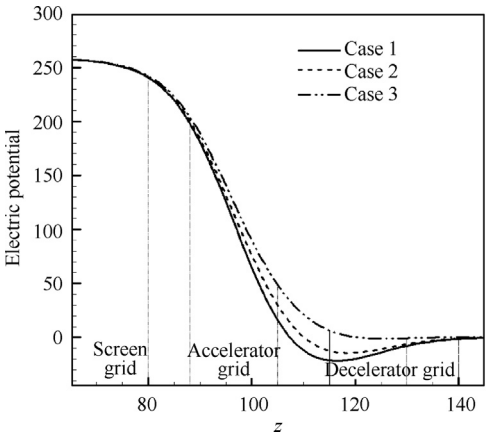

Fig. 9 Potential distribution of grid aperture axis.

3.2. Characteristics and mechanisms of cylindrical erosion and chamfer erosion

Numerical simulations were used to investigate the aperture barrel erosion induced by CEX ions after 1000 h of operation in each case. CEX ions in each case are traced to study their contributions on erosion. Fig. 10 illustrates the accelerator grid aperture barrel erosion rate for three cases. In Fig. 10(a), which is the initial stage of cylindrical erosion, CEX ions primarily erode the upstream area of the aperture barrel. In Fig. 10(b), which is the final stage of cylindrical erosion, the upper part of the accelerator grid aperture barrel is hardly eroded, and the erosion mainly occurs in the middle of the aperture barrel. In Fig. 10(c), which is the chamfer erosion phase, CEX ions only hit the downstream area of the accelerator grid.

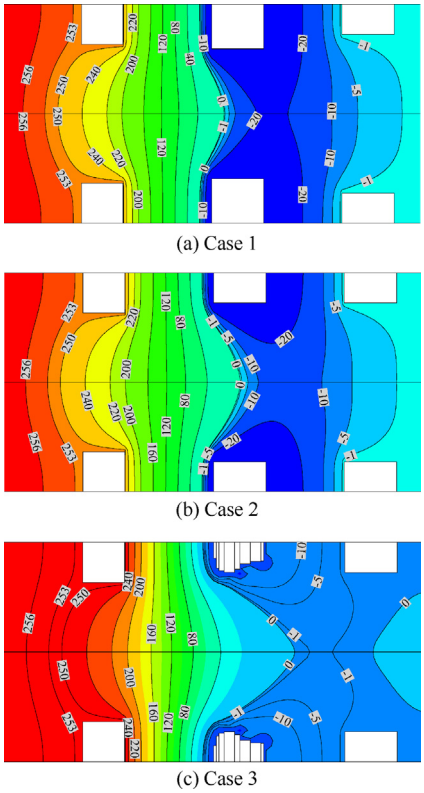

(a) Case 1

(b) Case 2

(c) Case 3

Fig. 8 Potential distribution of sheath structure and grid.

Table 6 summarizes the data for all CEX ions eroding accelerator grid aperture barrel (the data in Table 6 has been recovered from dimensionless), including mean erosion rate $\bar{R}_{\mathrm{E}}$, mean CEX ion impingement current density $\bar{J}$, mean incident energy $\bar{E}$, and mean incident angle $\bar{\theta}$. From Fig. 10 and Table 6, the maximum and mean erosion rate gradually decrease. This is because in the erosion process, with the transformation of the AEM, the negative potential region is gradually becoming smaller, so the number of CEX ions that can be attracted is also reduced. This is also demonstrated by the change in mean CEX ion impingement current density in Table 6. Both the incident energy and angle are related to the motion of the CEX ions and will be discussed later.

In order to further explore the erosion mechanism and characteristics, the generation locations of CEX ions were reproduced. Fig. 11 illustrates the generation locations of all CEX ions within the simulation domain, and Fig. 12 shows the generation locations of CEX ions that cause the accelerator grid barrel erosion. In addition, the mean number density of CEX ions is also counted in Table 7, where $\bar{n}_{\mathrm{cex\_tot}}$ is the mean number densities of all CEX ions and $\bar{n}_{\mathrm{cex\_acc}}$ is the CEX ions responsible for accelerator grid barrel erosion in three cases.

In Fig. 11, the CEX ions in the simulation domain are mainly distributed upstream of the screen grid, and inside or downstream of the accelerator grid aperture. And the transformation of AEM has no effect on the generation distribution of all CEX ions. It can be seen from Table 7 that in the cylindrical erosion phase, $\bar{n}_{\mathrm{cex\_tot}}$ is basically unchanged, while it decreases slightly in the chamfer erosion phase. Comparing Fig. 12(a) and Fig. 12(b), we can see that, in the cylindrical erosion phase, the generation locations of the CEX ions that cause the barrel erosion of the accelerator grid mainly include the region from the accelerator grid upstream to the decelerator grid downstream. In Fig. 12(c), the special erosion morphology in the chamfer erosion phase has a great influence on the generation locations of the CEX ions that cause barrel erosion. At this time, these CEX ions are mainly located in the aperture region of the decelerator grid. Moreover, $\bar{n}_{\mathrm{cex\_acc}}$ is gradually reduced as the erosion progresses in Table 7, which is consistent with the analysis of erosion characteristics above.

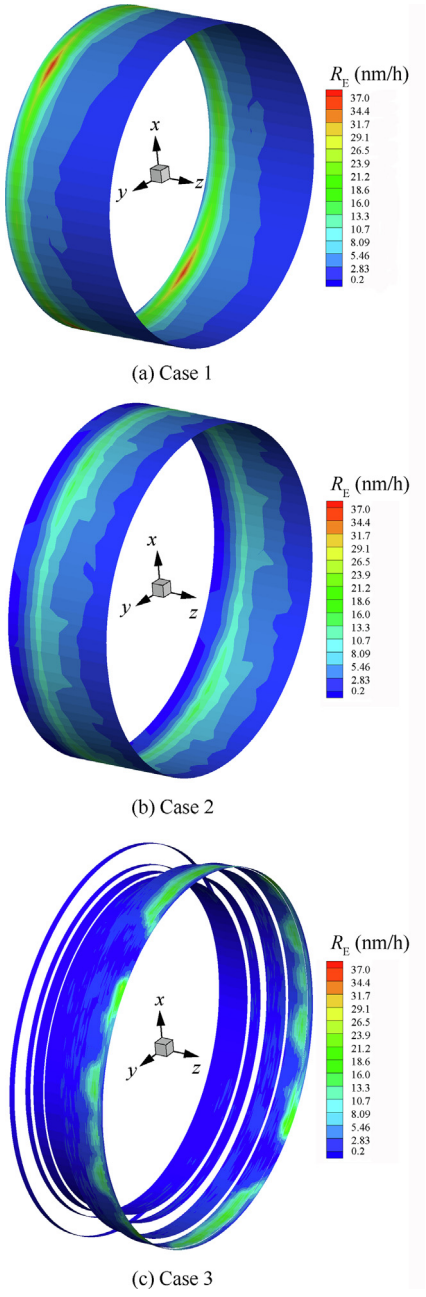

Fig. 10 Erosion rate of accelerator grid aperture surface.

Table 6 Data for all CEX ion erosion accelerator grid aperture barrel.

Case No.	$\bar{R}_E$(nm/h)	$\bar{J}$(A/m^2)	$\bar{E}$(eV)	$\bar{\theta}$(°)
1	5.88	5.03×10^{-2}	164.97	24.02
2	4.23	3.61×10^{-2}	180.14	18.24
3	1.47	1.56×10^{-2}	71.94	13.90

For the convenience of analysis, we divide the CEX ions causing barrel erosion into four regions according to their generation locations: the region upstream of the screen grid and within its aperture (Region 1), the region from the downstream end of the screen grid to the upstream end of the decelerator grid (Region 2), the region within the aperture of the decelerator grid (Region 3), and the region downstream of the decelerator grid (Region 4). The schematic diagram of regional division is shown in Fig. 13. Fig. 14 summarizes the changes in the relevant erosion data, where all variables have the same meaning and units as in Table 6.

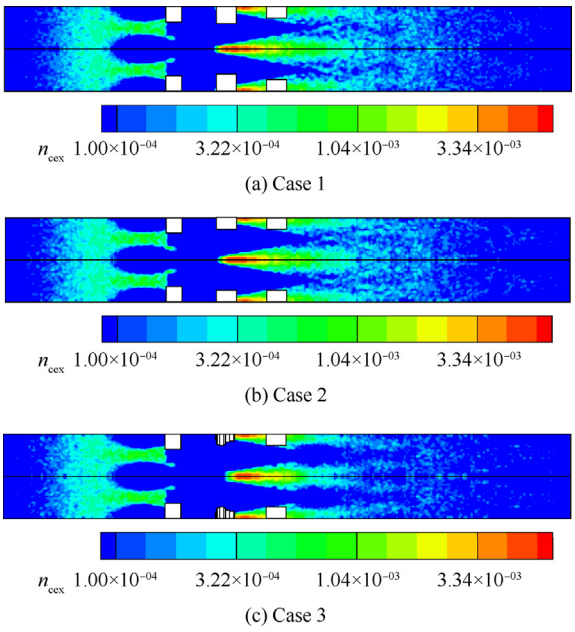

Fig. 11 Original locations of all CEX ions.

Fig. 14(a) presents the mean erosion rate $\bar{R}_E$ for different regions in three cases. According to Fig. 14(a), the trend of erosion rate changes is the same in different erosion phases. Among them, the erosion rate of Region 4 is the largest. For each region, the erosion rate decreases as the erosion progresses. The erosion rate is related to the incident energy and angle of CEX ions, and the changes in the mean incident energy and angle of each region in each case need to be explained in conjunction with the trajectory of CEX ions. Therefore, we recorded the generation position and velocity of the CEX ions eroding the accelerator grid aperture barrel and reproduced their trajectory. Fig. 15 presents the CEX ion trajectories of the four regions in the three cases. For the sake of clarity, only a few CEX ions are shown in the figure.

Fig. 14(b) shows that the mean incident energy of Case 1 and Case 2 has the same trend, both decreasing and then increasing. Observing the CEX ion trajectory of Case 1, we can find that the CEX ions at Region 1 will move downstream first, and then reflow to hit the accelerator grid aperture barrel, as shown in Fig. 15(a). In Fig. 12(a), the generation position of this part of CEX ions is mainly located upstream of the accelerator grid aperture. Combining Fig. 8(a) with Fig. 9, we can find that the CEX ions here are mainly located in the region where the potential is close to 0 or the negative potential value is low. Affected by the downstream negative potential region, these CEX ions will move downstream. At the same time, attracted by the accelerator grid, the CEX ions will eventually hit the accelerator grid aperture barrel. For Regions 2–4, since

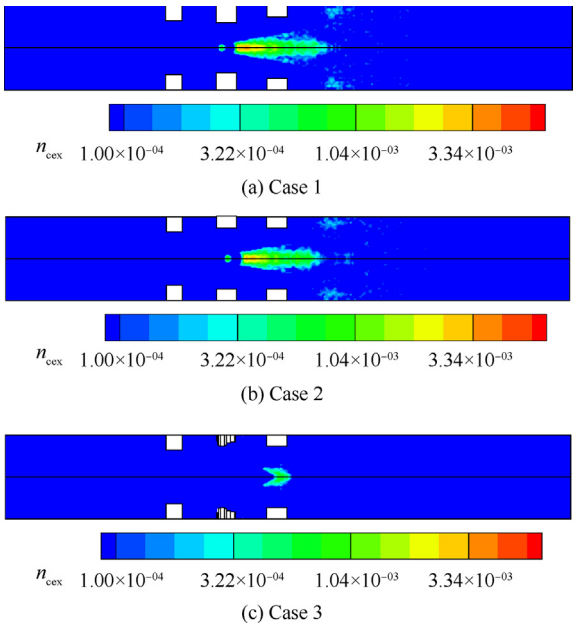

Fig. 12 Original locations of CEX ions that cause aperture barrel erosion.

Table 7 CEX ion mean number density.

Case No.	$\bar{n}_{cex\_tot}$	$\bar{n}_{cex\_acc}$
1	1.96×10^{-4}	4.07×10^{-5}
2	1.95×10^{-4}	3.62×10^{-5}
3	1.70×10^{-4}	3.74×10^{-6}

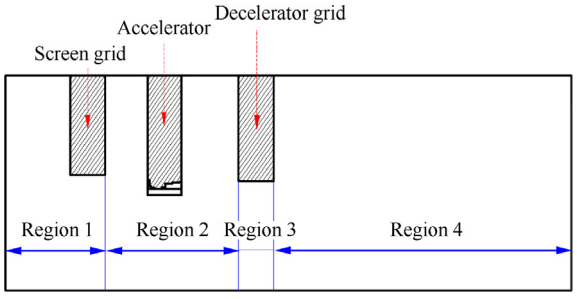

Fig. 13 Regional division.

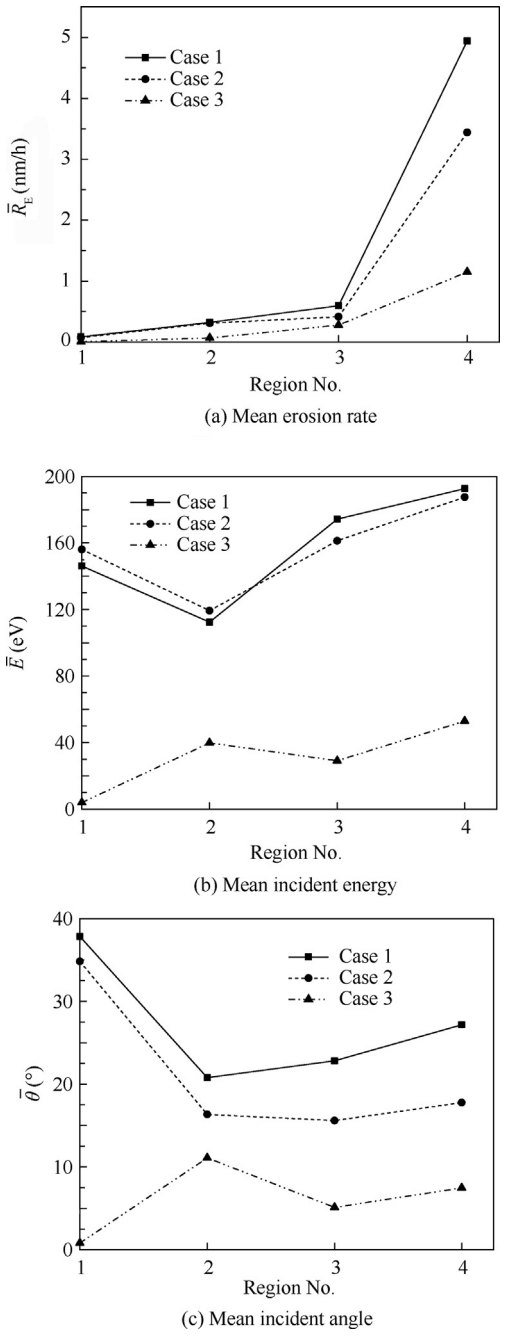

Fig. 14 Data for CEX ion from different regions.

the potential environment of CEX ions is different from that in Region 1, these CEX ions will be directly attracted by the accelerator grid and hit it, that is, the CEX ion back-streaming. The generation positions of CEX ions in different regions are different, and the energy obtained by CEX ions is related to the potential difference between the initial and final positions. Therefore, the mean incident energy from Region 2 to Region 4 is increasing. However, the CEX ions in Region 1 will undergo a process of first acceleration, then deceleration, and finally acceleration. It can be considered that its "back-streaming position" is located in the region where its velocity decelerates to 0 m/s during the movement, probably near the decelerator grid, so the mean incident energy of Region 1 is higher than that of Region 2, but lower than that of Region 3. For Case 2, the trajectory variation of CEX ions in each region is similar to that of Case 1, as shown in Fig. 15 (b), so the analysis will not be repeated here.

For Case 3, the mean incident energy varies significantly, as shown in Fig. 14(b). First of all, the mean incident energy in Region 1 is close to 0 eV. Combining Fig. 11(c) with Fig. 12 (c), we can find that CEX ions do exist in the aperture of the accelerator grid, but these CEX ions no longer erode the aperture barrel of the accelerator grid. In order to study the behavior of CEX ions here, we randomly took out a small amount of CEX ions in their generation region and recorded their motion trajectories, as shown in Region 1 in Fig. 15(c). Combining

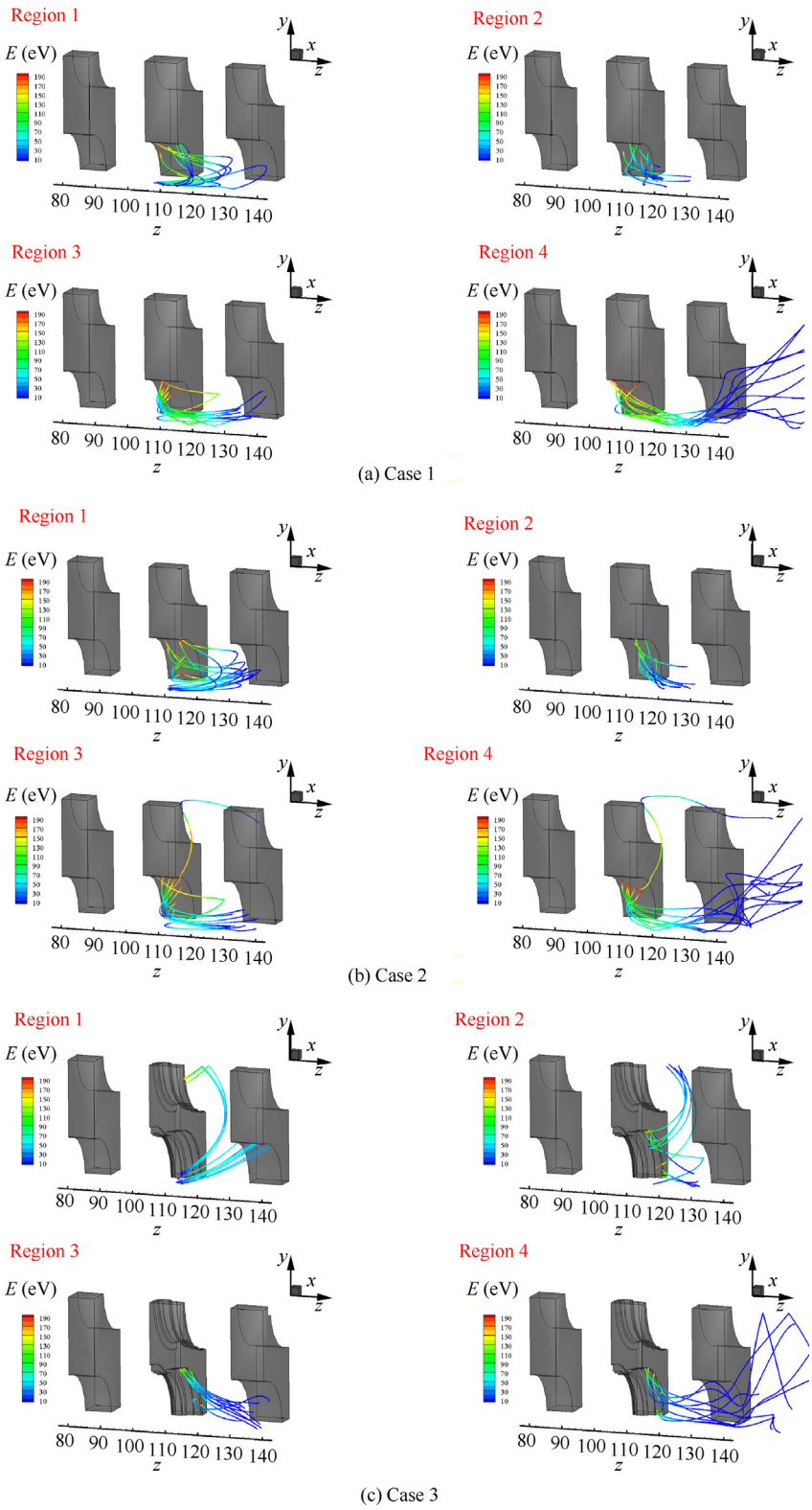

Fig. 15 Trajectories of CEX ions.

Fig. 8 with Fig. 9, we can find that the CEX ions of Region 1 in Case 3 are located in the positive potential region. Similar to the Region 1 in Case1 and Case 2, this part of CEX ions will be attracted by the negative potential near the downstream and accelerator grid, and move downstream at the same time to the accelerator grid. However, due to the transformation of the AEM, the influence of the negative potential of the accelerator grid is sharply reduced, causing some CEX ions

in Region 1 in Case 3 to break away from the attraction of the accelerator grid and finally erode the aperture barrel of the decelerator grid. The other part of the CEX ions ran to the vicinity of the adjacent hole and was bounced to the end face of the accelerator grid.

Without considering Region 1, the mean incident energy of different regions in the chamfer erosion phase will decrease and then increase. For each erosion phase, in addition to the CEX ions in its own aperture eroding the accelerator grid aperture barrel, the CEX ions from the adjacent apertures also cause barrel erosion, as shown in Region 3 and Region 4 in Fig. 15(b), and Region 2 in Fig. 15(c). Table 8 summarizes the percentage of CEX ions from adjacent apertures in each region for each case. Firstly, in Table 8, Region 4 has a large proportion of CEX ions from adjacent apertures, and the proportion will increase as the erosion progresses. Its ion trajectory is shown in Region 4 in Fig. 15(b). Observing the trajectory, we can see that the CEX ions from the adjacent apertures have to be decelerated to the barrel of the adjacent apertures before being accelerated to hit the own aperture, so the incident energy of the CEX ions from the adjacent aperture is substantially equal to or slightly lower than that from the own aperture. In other words, for Region 4, CEX ions from adjacent apertures do not affect the mean incident energy change. In Case 1 and Case 2, the proportion of CEX ions from adjacent apertures increases in all regions as the erosion progresses. Among them, for Regions 1, 2 and 3, the proportion is lower and has little effect on the mean incident energy. Hence, for the cylindrical erosion phase, the CEX ions located in Regions 1–3 that cause the barrel erosion mainly come from the own apertures. In Case 3, the proportion of CEX ions from adjacent apertures in Region 1 and Region 3 is almost 0, but for Region 2, the proportion rises sharply. In this region, the CEX ions from the adjacent apertures will be directly accelerated to hit the own aperture, and the incident energy of the CEX ions from the adjacent apertures will be higher than the CEX ions from the own aperture, as shown in Fig. 15(c) Region 2. So in Case 3, the mean incident energy of Region 2 is higher than that of Region 3 due to the increased contribution of CEX ions from adjacent apertures. The mean incident energy of Region 4 is higher than that of Region 3, and the reason is the same as the cylindrical erosion phase, i.e., the potential difference at different original positions.

In Fig. 14(b), comparing Case 1 and Case 2, we can find that the mean incident energy of each region does not change much, but in Case 3, the mean incident energy of each region is greatly reduced. In the cylindrical erosion phase, AEM can still remain cylindrical, and the transformation of AEM mainly affects the potential distribution near the accelerator grid, that is, the potential distribution near Region 1 and Region 2. Therefore, the mean incident energy of CEX ions in Region 1 and Region 2 of Case 1 is lower than that of Case 2, while those of Region 3 and Region 4 are opposite. However, in the chamfer erosion phase, the potential of all regions increases to a certain extent due to the special morphology, so the potential difference decreases, and the energy obtained by the CEX ions also decreases.

Fig. 14(c) presents the variation of the mean incidence angle for different regions in different erosion phases. For each region, the mean incidence angle keeps decreasing as the erosion progresses. As the erosion time increases, the barrel of the eroded aperture will be parallel to the trajectories of most CEX ions, so the mean incidence angle decreases.

Table 8 Proportion of CEX ions from adjacent apertures.

Region No.	Proportion of CEX ions (%)		
	Case 1	Case 2	Case 3
1	1.49	7.26	0
2	0.03	0.11	59.14
3	4.58	5.82	0.13
4	29.08	35.96	40.71

4. Conclusions

In this paper, the accelerator grid morphologies under extreme conditions are reconstructed, the IFE-PIC-MCC method is used to study the transport process of beam ions and Charge Exchange (CEX) ions in the grid system. The generation position and movement trajectory of CEX ions are reproduced, and the barrel erosion characteristics and mechanisms of the accelerator grid under extreme conditions are explored in combination with the grid erosion evaluation model. Main conclusions are drawn as follows:

(1) The transformation of the AEM has no effect on the beam ions. As the erosion progresses, the erosion position of the CEX ion moves downstream along the grid aperture axis direction, and the erosion range becomes narrower.
(2) The transformation of the AEM only affects the local electric field distribution, and has no effect on the plasma sheath. In the cylindrical erosion phase, it only affects the potential distribution around the accelerator grid, but in the chamfer erosion phase, this impact will spread downstream of the decelerator grid. And as the erosion progresses, the negative potential area gradually decreases.
(3) The transformation of the AEM has no effect on the generation positions of all CEX ions, but it has a significant effect on the distribution of CEX ions that cause barrel erosion. In the cylindrical erosion phase, the distribution of CEX ions does not change, while in the chamfer erosion stage, the distribution of CEX ions is reduced to the region near the aperture of the decelerator grid. And the mean number density of CEX ions causing barrel erosion is gradually reduced as the erosion progresses.
(4) Regardless of the erosion phase, the erosion rate of the CEX ions located downstream of the decelerator grid is the largest. The erosion rate is related to the mean incident energy and angle, and their variation is closely related to the ion trajectory. In the cylindrical erosion phase, the mean incident energy of CEX ions in each region does not change much, and will decrease and then increase with the change of regions, which is mainly caused by the special trajectory of CEX ions in Region 1. In the chamfer erosion phase, the mean incident energy of each region is greatly reduced, and the CEX ions in Region 1 no longer cause barrel erosion, but erode the end face of the accelerator grid and the aper-

ture barrel of the decelerator grid. And the mean incident energy of Region 2 increases due to the contribution of CEX ions from adjacent apertures. As the erosion time increases, the barrel of the eroded aperture will be parallel to the trajectories of most CEX ions, and the mean incidence angle decreases.

Declaration of Competing Interest

The authors declare that they have no known competing financial interests or personal relationships that could have appeared to influence the work reported in this paper.

Acknowledgments

This work was supported by the National Key R & D Program of China (No. 2020YFC2201100), the National Key R & D Program for Intergovernmental International Scientific and Technological Innovation Cooperation, China (No. 2021YFE0116000), the National Natural Science Foundation of China (Nos. 12175032, 12102082, 12275044, 12211530449), the Fundamental Research Funds for the Central Universities of China (Nos. DUT21GJ206 and DUT22QN232), the S & T Program of Hebei, China (Nos. YCYZ202201, 216Z1901G and 206Z1902G), the S & T Innovation Program of Hebei, China (Nos. SJMYF2022X18 and SJMYF2022X06); the Advanced Space Propulsion Laboratory of BICE and Beijing Engineering Research Center of Efficient and Green Aerospace Propulsion Technology, China (No. LabASP-2020-06); and the Funded by Science and Technology Project of Hebei Education Department, China (No. ZC2023144).

References

1. Lu C, Xia GQ, Sun B, et al. Confinement characteristic of primary electrons with the variation of channel width in the discharge chamber of annular ion thruster. *Chin J Aeronaut* 2021;**34**(5):79–92.
2. Ning ZX, Liu CG, Zhu XM, et al. Diagnostic and modelling investigation on the ion acceleration and plasma throttling effects in a dual-emitter hollow cathode micro-thruster. *Chin J Aeronaut* 2021;**34**(12):85–98.
3. Boyd I, Crofton M. A computational study of grid erosion through ion impact. Reston: AIAA; 2000. Report No.: AIAA-2000-3664.
4. Peng XH, Ruyten WM, Friedly VJ, et al. Particle simulation of ion optics and grid erosion for two-grid and three-grid systems. *Rev Sci Instrum* 1994;**65**(5):1770–3.
5. Boyd I, Crofton M. A computational study of grid erosion through ion impact. Reston: AIAA; 2000. Report No.: AIAA-2000-3664.
6. Emhoff J, Boyd I. Grid erosion modeling of the next ion thruster optics. Reston: AIAA; 2003. Report No.: AIAA-2003-4868.
7. Wang J, Polk J, Brophy J, et al. Three-dimensional particle simulations of ion-optics plasma flow and grid erosion. *J Propul Power* 2003;**19**(6):1192–9.
8. Kafafy R, Wang J. Whole ion optics simulations of a subscale gridlet using a hybrid-grid IFE-PIC code. Reston: AIAA; 2004. Report No.: AIAA-2004-3783.
9. Kafafy R. Immersed finite element particle-in-cell simulations of ion propulsion[dissertation]. Blacksburg: Virginia Polytechnic Institute and State University; 2005.
10. Kafafy R, Wang J. A hybrid grid immersed finite element particle-in-cell algorithm for modeling spacecraft–plasma interactions. *IEEE Trans Plasma Sci* 2006;**34**(5):2114–24.
11. Cao HJ, Chu YC, Wang EM, et al. Numerical simulation study on barrel erosion of ion thruster accelerator grid. *J Propuls Power* 2015;**31**(6):1785–92.
12. Brophy JR. Propellant throughput capability of the dawn ion thrusters. *30th international electric propulsion conference*. 2007. p.17-20.
13. Wirz RE, Anderson JR, Katz I. Time-dependent erosion of ion optics. *J Propuls Power* 2011;**27**(1):211–7.
14. Lu C, Xia G, Sun B, et al. A particle model of ion thruster plume Mo source based on grid erosion. *Acta Astronaut* 2020;**177**:217–31.
15. Sun MM, Wang L, Yang JT, et al. Study of the key factors affecting the triple grid lifetime of the LIPS-300 ion thruster. *Plasma Sci Technol* 2018;**20**(4):045504.
16. Tskhakaya D, Matyash K, Schneider R, et al. The particle-in-cell method. *Contrib Plasma Phys* 2007;**47**(8–9):563–94.
17. Birdsall CK, Langdon AB. *Plasma physics via computer simulation*. Boca Raton: CRC Press; 2018.
18. Hockney RW, Eastwood JW. *Computer simulation using particles*. Boca Raton: CRC Press; 2021.
19. Tajmar M, Wang J. Three-dimensional numerical simulation of field-emission-electric-propulsion neutralization. *J Propuls Power* 2000;**16**(3):536–44.
20. Rapp D, Francis WE. Charge exchange between gaseous ions and atoms. *J Chem Phys* 1962;**37**(11):2631–45.
21. Vahedi V, Surendra M. A Monte Carlo collision model for the particle-in-cell method: applications to argon and oxygen discharges. *Comput Phys Commun* 1995;**87**(1–2):179–98.
22. Lu C, Yang Z, Bai JW, et al. Three-dimensional immersed finite-element method for anisotropic magnetostatic/electrostatic interface problems with nonhomogeneous flux jump. *Int J Numer Methods Eng* 2020;**121**(10):2107–27.
23. Lu C, Wan J, Cao Y, et al. A fully decoupled iterative method with three-dimensional anisotropic immersed finite elements for Kaufman-type discharge problems. *Comput Methods Appl Mech Eng* 2020;**372**:113345.
24. Yamamura Y, Itikawa Y, Itoh N. Angular dependence of sputtering yields of monatomic solids. Nagoya: Institute of Plasma Physics, Nagoya University;1983. Report No.: IPPJ-AM-26.
25. Rosenberg D, Wehner GK. Sputtering yields for low energy He^+-, Kr^+-, and Xe^+-ion bombardment. *J Appl Phys* 1962;**33**(5):1842–5.
26. Lu C, Luo Y, Xia GQ, et al. Numerical study of the grid erosion of field emission electric propulsion. *Plasma Sci Technol* 2021;**23**(10):104001.